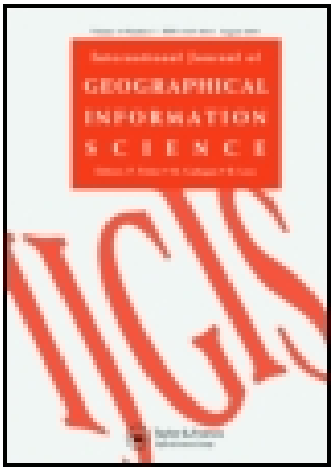

International Journal of Geographical Information Science

Publication details, including instructions for authors and subscription information:
http://www.tandfonline.com/loi/tgis20

Fusion of multi-scale DEMs using a regularized super-resolution method

Linwei Yue[a], Huanfeng Shen[bc], Qiangqiang Yuan[cd] & Liangpei Zhang[ac]

[a] The State Key Laboratory of Information Engineering in Surveying, Mapping and Remote Sensing, Wuhan University, Wuhan, P.R. China

[b] School of Resource and Environmental Science, Wuhan University, Wuhan, P.R. China

[c] Collaborative Innovation Center of Geospatial Technology, Wuhan University, Wuhan, P.R. China

[d] School of Geodesy and Geomatics, Wuhan University, Wuhan, P.R. China

Published online: 10 Jul 2015.

To cite this article: Linwei Yue, Huanfeng Shen, Qiangqiang Yuan & Liangpei Zhang (2015): Fusion of multi-scale DEMs using a regularized super-resolution method, International Journal of Geographical Information Science, DOI: 10.1080/13658816.2015.1063639

To link to this article: http://dx.doi.org/10.1080/13658816.2015.1063639

International Journal of Geographical Information Science, 2015
http://dx.doi.org/10.1080/13658816.2015.1063639

Taylor & Francis
Taylor & Francis Group

Fusion of multi-scale DEMs using a regularized super-resolution method

Linwei Yue[a], Huanfeng Shen[b,c]*, Qiangqiang Yuan[c,d] and Liangpei Zhang[a,c]*

[a]*The State Key Laboratory of Information Engineering in Surveying, Mapping and Remote Sensing, Wuhan University, Wuhan, P.R. China;* [b]*School of Resource and Environmental Science, Wuhan University, Wuhan, P.R. China;* [c]*Collaborative Innovation Center of Geospatial Technology, Wuhan University, Wuhan, P.R. China;* [d]*School of Geodesy and Geomatics, Wuhan University, Wuhan, P.R. China*

(*Received 25 September 2014; accepted 15 June 2015*)

The digital elevation model (DEM) is a significant digital representation of a terrain surface. Although a variety of DEM products are available, they often suffer from problems varying in spatial coverage, data resolution, and accuracy. However, the multi-source DEMs often contain supplementary information, which makes it possible to produce a higher-quality DEM through blending the multi-scale data. Inspired by super-resolution (SR) methods, we propose a regularized framework for the production of high-resolution (HR) DEM data with extended coverage. To deal with the registration error and the horizontal displacement among multi-scale measurements, robust data fidelity with weighted L_1 norm is employed to measure the conformance of the reconstructed HR data to the observed data. Furthermore, a slope-based Markov random field (MRF) regularization is used as the spatial regularization. The proposed method can simultaneously handle complex terrain features, noises, and data voids. Using the proposed method, we can reconstruct a seamless DEM data with the highest resolution among the input data, and an extensive spatial coverage. The experiments confirmed the effectiveness of the proposed method under different cases.

Keywords: multi-scale DEMs; data fusion; regularized framework; super-resolution

1. Introduction

As a popular digital representation of cartographic information, digital elevation models (DEMs) are grids with regularly spaced elevation values in a raster form. Due to their simple data structure and widespread availability, DEMs have been broadly applied in scientific fields such as ecology (Kellndorfer *et al*. 2004), agriculture (Fu and Rich 2002), and hydrological modeling (Passalacqua *et al*. 2010, Huang *et al*. 2014, Zheng *et al*. 2015). There are a variety of DEM products available with different sources. Early DEM data were mainly generated by digitizing existing topographic maps. However, they can now be directly derived using remote sensing and photogrammetric techniques (Erdogan 2009). Efforts have been directed toward generating DEMs from digital stereo images acquired by satellite-based sensor systems, for example, the advanced space-borne thermal emission and reflection radiometer (ASTER) global digital elevation model (GDEM). Nevertheless, remote sensing images are often sensitive to weather condition and terrain types (Hirano *et al*. 2003).

*Corresponding authors. Email: shenhf@whu.edu.cn, zlp62@whu.edu.cn

Compared with other satellite-based techniques, the synthetic aperture radar (SAR) remote sensing technique can provide high-resolution (HR) elevation data in all weather conditions, both day and night, at a global scale (Chen *et al*. 2009). The famous representative product is the Shuttle Radar Topography Mission (SRTM) 90 m global DEM (Hormann *et al*. 2003). Additionally, ground-based or air-borne automatic laser scanners can provide very high resolution elevation data and are suitable for relatively small areas (Darboux and Huang 2003, Zhou and Zhu 2013).

Variations in quality always exist among different DEM products. For example, DEMs derived from space-borne sensors generally provide data over broad areas, but the inadequate spatial resolution may result in a limited application for surface terrain analysis. Meanwhile, interferometric SAR-derived DEMs acquired from air-borne platforms have prominent advantages in the spatial resolution. Nevertheless, they often suffer from data voids or heavy noise, in addition to the narrow coverage due to the low altitude (Jhee *et al*. 2013).

Generally speaking, DEMs with a very high spatial resolution are usually limited in their spatial coverage or have data quality problems (e.g., data voids and noises) without any preprocessing, as well as the high cost of data acquisition; while, relatively low-resolution (LR) DEMs provide insufficient spatial information due to their restricted spatial representative ability. Based on these facts, many researchers have focused on the task of quality improvement of DEMs. A number of interpolation methods can be used to enhance the spatial information of a DEM on a sparse grid, for example, the bilinear, inverse distance weighted (IDW), spline, and kriging interpolation method based on geo-statistical theory (Liu 2008). However, finite information for interpolation will oversmooth the terrain surface, especially over the rough areas. Among the further studies, auxiliary data have been used to overcome the oversimplification in DEM densification. Chen *et al*. (2013) made use of multispectral information to reveal the actual surface reflection properties, and thus generated a higher-resolution DEM using the shape-from-shading (SFS) technique. Robinson *et al*. (2014) reconstructed a new DEM product called 'EarthEnv-DEM90' by combining multi-scale DEM datasets (90 m and 30 m). The main contribution of this work was to extend the coverage of current data, and improve the data quality by filling data voids and suppressing the noise, but the spatial resolution of the final product was only 90 m.

Moreover, researchers have also tried to introduce fusion ideas into DEM reconstruction. Karkee *et al*. (2008) attempted to fuse SRTM and ASTER GDEM data in the frequency domain to fill the data voids and improve the overall accuracy of the fused data. Jhee *et al*. (2013) adopted multi-scale modeling for DEMs to fill the voids in HR data, while a multi-scale Kalman smoother (MKS) based on the Markov property was used to remove blocky artifacts. In addition, Jiang *et al*. (2014) tried to fuse DEMs derived from two HR InSAR data pairs acquired from the descending and ascending orbits, employing a maximum likelihood fusion scheme to remove the voids in the fused data. All the methods mentioned are inadequate for the use of supplementary DEM information with different resolutions, coverage, and vertical accuracies. Additionally, they have difficulty in simultaneously processing multiple problems, including noise, data voids, and resolution enhancement.

To overcome these limitations, we introduce the concept of super-resolution (SR). SR is a technique which takes resolution limitation and common degradation factors into consideration at the same time. Image SR can produce an image with higher resolution using the redundant information among multiple low-resolution images (Park *et al*. 2003).

It was first addressed by Tsai and Huang to improve the spatial resolution of Landsat TM images with relative sub-pixel motion (Tsai and Huang 1984). Their methods deal with the problem in the frequency domain, which is extremely sensitive to model errors. Therefore, methods in the spatial domain have become more popular in recent years, including iterative back projection (IBP) (Irani and Peleg 1991), projection onto convex sets (POCS) (Zhang and Zhou 2011), and a group of regularized variational methods (Park *et al*. 2003; Ng *et al*. 2007b; Zhang *et al*. 2007, Zeng and Yang 2013). Among these methods, Bulyshev *et al*. (2011) attempted to employ a back projection (BP) method for the processing of multiple three-dimensional Flash LiDAR DEM data. However, this method has only been tested on simulated data, ignoring the possible inconsistency between multi-sensor and multi-scale DEMs.

Early SR methods mainly assumed that all the LR images have the identical spatial resolution. Nevertheless, multi-scale data are common in the real cases. Thus, multi-scale SR for multiple image reconstruction with different resolutions started to be focused (Joshi *et al*. 2005; Ng *et al*. 2007a; Tian and Yap 2013, Song *et al*. 2015). The key point of multi-scale SR is to solve the tradeoff between spatial resolution and coverage, and obtain an image with high-resolution and wide coverage. Inspired by the SR methods, we propose a regularized framework for multi-source and multi-scale DEM fusion. Despite the spatial resolutions, other factors such as horizontal displacements, registration errors, data voids, as well as the relative vertical discrepancies among the multi-source data should also be considered in DEM fusion (Fisher and Tate 2006).

The motivation behind the proposed multi-scale fusion algorithm is to obtain a seamless integration of data from DEMs with multiple resolutions, and thus reconstruct the desired data with the highest resolution and extensive coverage among the input data, as shown in Figure 1. The result was reconstructed using the LR data with maximum coverage as fundamental information and partially HR information as a constraint.

In view of this, there are three main problems we need to settle. First, the proposed method conducted DEM fusion using the highest-resolution dataset as the referenced coordinate datum. Although different DEM datasets have overlapped areas, there will be relative horizontal displacements between them (Robinson *et al*. 2014). Moreover, the errors in the registration process will be included in the proposed model. However, the horizontal errors are complicated and hard to

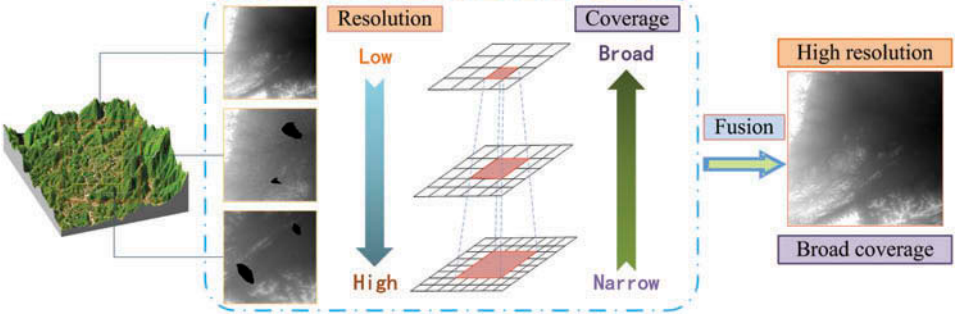

Figure 1. Fusion of DEM data with different scales and different spatial coverage.

measure. Considering inaccurate error estimation will bring unmanageable disturbance to our model, sub-pixel horizontal errors are not considered separately, but included as the influence of vertical errors in the article. Thus, the proposed algorithm adopts L_1 norm (Farsiu *et al*. 2004) for the data fidelity in the objective function. Furthermore, using the relative residuals between the input multi-scale data and the desired data (the reconstructed result), we compute the contribution of each data to construct the weighted objective function, according to the quality of the multi-scale data. Second, data voids and anomalies (pixels with gross error) caused by radar shadowing, unwrapping errors, and low-backscattering targets are always challenges for the data users (Reuter *et al*. 2007). This algorithm is capable of filling data voids by detecting the invalid pixels, including the missing values and the anomalies caused by production differences and terrain changes. Lastly, regularization should be designed especially for DEMs to represent their intrinsic characteristics. Markov random field (MRF) regularization is employed to preserve the spatial neighborhood continuity of the reconstructed DEM. To better describe the terrain surface, slope information was utilized to analyze the spatial distribution of the landscapes, thereby handling the flat regions and the edges in a spatially adaptive manner, both for inconsistent pixels detection and regularization construction. Unlike the traditional methods for DEM enhancement, we integrate resolution enhancement, noise suppression, and data voids filling into a universal framework.

The rest of this paper is organized as follows. Section 2 gives a specific and detailed description of the proposed method. The experiments in multi-scale DEM fusion, including two simulated and three real data experiments, are presented in Section 3. This section also includes an analysis of the constructed data. Lastly, Section 4 is the conclusion.

2. Method

2.1. *The generative model*

To get the desired reconstructed DEM from input multi-scale DEM data using a regularized method, we should first describe the relationship among them. We assume that the input DEMs can be acquired from the desired HR data with extensive coverage through a degradation process. It has been mentioned that we want to obtain HR data with the same coverage as the lowest-resolution input data ($N_1 \times N_2$) and the same resolution as the highest-resolution input data. Therefore, the size of the reconstructed HR DEM ($HN_1 \times HN_2$) can be calculated as

$$HN_1 = N_1 \times \frac{g_1}{g_K}, HN_2 = N_2 \times \frac{g_1}{g_K} \tag{1}$$

where g_1 and g_K represent the lowest and highest resolutions, respectively, among the total K data participating in the fusion. For example, if we want to fuse three overlapped DEM datasets with resolutions of 10 m (70 × 70), 20 m (60 × 60), and 30 m (50 × 50), then the reconstructed dataset is a seamless DEM with a 10 m resolution and a size of 150 × 150.

According to the DEM generation process, the different data scales are determined by the sampling intervals. Moreover, the values in a gridded DEM are assumed to be the height of a certain area on the earth's surface above a defined datum. Based on this

concept, it is possible to revisit each point and repeat the measurement (Fisher and Tate 2006). All the measurements are usually subject to errors, which appear as noise in the elevation data. In this paper, we consider the error model as random with gross errors excluded (Fisher and Tate 2006, Wechsler 2007, Gallant 2011). Thus, we define the generation model for a multi-scale DEM as

$$\boldsymbol{y}_k = \boldsymbol{O}_k \boldsymbol{D}_k \boldsymbol{M}_k \boldsymbol{u} + \boldsymbol{n}_k \tag{2}$$

As $N_{1k} \times N_{2k}$ is defined as the size of the kth input data, $HN_1 \times HN_2$ is set as the size of the reconstructed HR data defined in Equation (1). In Equation (2), $\boldsymbol{u}$ is the vector form of the reconstructed DEM with a size of $HN_1HN_2 \times 1$, whereas $\boldsymbol{y}_k$ is the vector form of the kth input data with size of $N_{1k}N_{2k} \times 1$. After registering $\boldsymbol{u}$ and the corresponding degraded data to the reference coordinate datum, $\boldsymbol{M}_k$ ($HN_1HN_2 \times HN_1HN_2$) describes the translation matrix. As shown in Figure 2, the resampled LR data sometimes had sub-pixel misalignment with the referenced HR grid. To avoid the extra errors brought by the geometric sampling, it was better to directly move its pixels into the HR grid. By multiplying $\boldsymbol{M}_k$ by $\boldsymbol{u}$, we slightly adjust the HR grid for alignment with the input data with the highest spatial resolution. $\boldsymbol{D}_k$ ($N_{1k}N_{2k} \times HN_1HN_2$) is the down-sampling matrix, and $\boldsymbol{n}_k$ ($N_{1k}N_{2k} \times 1$) represents the random error. Given that the coverage for each observed dataset differs, we define the cropping operator $\boldsymbol{O}_k$ ($N_{1k}N_{2k} \times N_{1k}N_{2k}$) as a diagonal matrix with the zero elements if the corresponding pixel was invalid or unobservable in the kth input data. It crops out the unobservable pixels from the HR data at an appropriate position after registration and re-sampling. Furthermore, invalid values, including voids and anomalies in the DEM, are also included in the unobservable matrix $\boldsymbol{O}_k$.

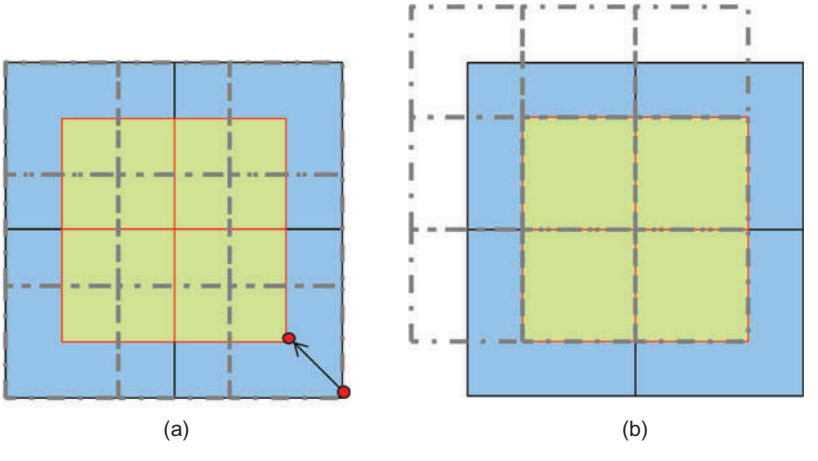

Figure 2. The translational relationship between the LR data and HR data. The blue grids (low resolution, wide spatial range) and green grids (referenced high resolution data grid with relatively narrow spatial coverage) represent the input data, whereas the gray dotted mesh indicate the reconstructed HR data.

2.2. The adaptive-weighted multi-scale regularized framework

Given the input multi-scale DEM data (known variables), we want to obtain a reconstructed HR DEM (unknown variable). Once the generative model is fixed, we can set the problem as an inverse process. To solve the ill-posed inverse problem, we choose the regularized framework for its advantages in adding prior information and simultaneously handling multiple degradation problems. Using the regularization techniques, the desired DEM data can be obtained by solving the following minimization function:

$$\hat{\boldsymbol{u}} = \arg\min\left[\sum_{k}^{K}\Psi(\boldsymbol{y}_k - \boldsymbol{A}_k\boldsymbol{u}) + \lambda R(\boldsymbol{u})\right] \tag{3}$$

where $\boldsymbol{A}_k = \boldsymbol{O}_k\boldsymbol{D}_k\boldsymbol{M}_k$. In this objective function, the first fidelity term $\Psi(\cdot)$ provides a constraint for the conformance of the reconstructed HR data to the observed LR data, in accordance with the model in Equation (2). The second term $R(\cdot)$ is the regularization, and we can keep the balance between the two competing terms by tuning the regularization parameter λ. Usually, a larger λ will cause a smoother terrain surface. A smaller λ can preserve the details better, but noise and other errors will also be kept.

2.2.1. The robust adaptive-weighted norm fidelity for DEM fusion

This section describes the fidelity model for the proposed framework. The main task is to determine the $\Psi(\cdot)$ in Equation (3). First, geometric registration should be implemented for datasets with different coordinate systems, and the specific registration strategy will be described in the experiments (Section 3.3). The motion vector for calculating the translation matrix $\boldsymbol{M}_k$ can then be easily acquired after registration, and the cropping region can also be obtained according to the coordinates. We should then detect the inconsistent pixels, which are common in DEM data. In general, data voids can be easily detected. However, sometimes severe pixels with gross errors whose information is completely invalid should also be regarded as missing values. Therefore, we detect these inconsistent pixels using a threshold for the difference between the corresponding values at pixel i in the multi-scale DEMs after geometric registration:

$$\left|y_k(i) - y_l^{'}(i)\right| < T \tag{4}$$

Here, $\boldsymbol{y}_l^{'}$ is the reference data after geometrically matching and re-sampling to $\boldsymbol{y}_k$. Generally speaking, DEMs with a higher vertical accuracy and better data integrity will be chosen as the reference data in Equation (4). The threshold T is usually set to be large enough, to guarantee that the invalid pixels are detected. Nevertheless, it is sometimes hard to achieve a balance between excluding the anomalies and preserving the useful HR information. We consider spatial information into this procedure, and the expression is modified to

$$\left|y_k(i) - y_l^{'}(i)\right| < T \times S_i \tag{5}$$

where $\boldsymbol{S}$ ($N_{1k}N_{2k} \times 1$) is the slope vector for $\boldsymbol{y}_k$. Then S_i represents the pixel's normalized slope value at pixel i with the location (m, n) in the corresponding DEM data in the form

of matrix, where $i = (n-1) \times N_{1k} + m$. Slope is one of the most significant surface morphological parameters, and there are a variety of algorithms for slope calculation (Zhou and Liu 2004). Considering the popularity and robustness to noise, we choose the third-order finite-difference weighted by reciprocal of squared distance (3FDWRSD) algorithm to calculate the slope information. Given $\boldsymbol{z}$ ($N_{1k}N_{2k} \times 1$) as the DEM data vector, the slope value at pixel (m, n) can then be defined as

$$\begin{aligned} S_i &= \arctan\sqrt{f_x^2 + f_y^2} \\ f_x &= \left(z_{i-N_{1k}-1} - z_{i-N_{1k}+1} + \sqrt{2}(z_{i-1} - z_{i+1}) + z_{i+N_{1k}-1} - z_{i+N_{1k}+1}\right) / \left(4 + 2\sqrt{2}\right) g_k \\ f_y &= \left(z_{i+N_{1k}+1} - z_{i-N_{1k}+1} + \sqrt{2}(z_{i+N_{1k}} - z_{i-N_{1k}}) + z_{i+N_{1k}-1} - z_{i-N_{1k}-1}\right) / \left(4 + 2\sqrt{2}\right) g_k \end{aligned} \tag{6}$$

where g_k is the DEM resolution, and the pixel location $i = (n-1) \times N_{1k} + m$.

After excluding the effect of the invalid pixels, there are two other problems that we need to settle. One of the issues is the horizontal errors. Errors occur in the planar (XY) coordinates due to the registration error. In addition, horizontal displacement is inevitable, even for data with the same coordinate datum. This will affect the vertical accuracy during the fusion process, because neighboring information will be used in the fusion process. It has been proved that the L_2-norm fidelity model results in a pixel-wise mean, while the L_1 model results in a pixel-wise median of all the measurements after motion compensation (Farsiu *et al*. 2004). For this reason, we adopt the L_1 norm rather than the L_2 norm for the fidelity, and thus deal with horizontal errors more robustly.

Another significant concern is the discrepancy between multi-scale DEMs. DEM products are acquired through various measurements and at different times. A variety of factors, such as the spatial scales, data collection techniques, and noises, can influence the data quality (Chaplot *et al*. 2006, Chen and Yue 2010). Furthermore, the quality for different areas of the same data product may be not stable. Based on this fact, we should consider weights in the construction, and assign larger weights for data with a better quality (Zhang *et al*. 2012). Thus, the objective function in Equation (3) can be rewritten as

$$\hat{\boldsymbol{u}} = \arg\min\left[\sum_k w_k \cdot \|(\boldsymbol{y}_k - \boldsymbol{A}_k\boldsymbol{u})\|_1^1 + \lambda R(\boldsymbol{u})\right] \tag{7}$$

where w_k represents the weight for the kth dataset. Then, how can we determine the weight for each DEM dataset?

According to Fisher and Tate (2006), the error of a given set of point measurements of a surface can be determined by comparison with reference data that is assumed to be error free. It is natural that we assume that the reconstructed data are more accurate. Therefore, we set the weight at the rth iteration on the basis of the residual as

$$w_k^{(r+1)} = K \frac{1/\log\left(1 + \left\|\boldsymbol{y}_k - \boldsymbol{A}_k\boldsymbol{u}^{(r)}\right\|_2\right)}{\sum_{k=1}^{K}\left[1/\log\left(1 + \|\boldsymbol{y}_k - \boldsymbol{A}_k\boldsymbol{u}^{(r)}\|_2\right)\right]} \tag{8}$$

This function determines the contribution of each DEM data in the fusion. The $\log(\cdot)$ function prevents the parameter being too sensitive, and the value of 1 ensures that the weight is non-negative.

2.2.2. Slope-adaptive Markov random field regularization

The selection of the regularization is a pivotal task in SR, because it will determine the spatial characteristics of the fused data. There are a variety of popular regularizations, such as the total variation (TV) model (Ng *et al*. 2007b), the MRF model (Pan and Reeves 2006), and the nonlocal-based models (Zhang *et al*. 2010).

MRFs are commonly used in image processing due to their good performance in modeling the contextual correlations between neighboring pixels. Two types of regularizations are popularly used, which are Gaussian-Markov random field (GMRF) and Huber-Markov random field (HMRF) regularization. GMRF tends to oversmooth the sharp edges and detailed information, while HMRF can overcome the criticism to a degree by spatial information classification (Li and Singh 2009).

As we know, measurements in DEMs are often affected by random noise, and can be even more obviously affected in low-relief areas where the shapes are subtle (Gallant 2011). An ideal regularization can relieve the trade-off between removing noise and preserving details. Inspired by MRF theory, we construct a spatially adaptive MRF regularization in the proposed method. Different norm functions are used for the constraint, and slope information is employed to measure the spatial information of the DEM.

Based on MRF theory, the regularization is used with the objective function as

$$R(\boldsymbol{u}) = \sum_{i} \sum_{t=1}^{\tau} \left\| d_c^t(u_i) \right\|_{p_i}^{p_i} \tag{9}$$

where $d_c^t(\cdot)$ is a coefficient operator for each clique c, and p_i denotes the pixel-wise adaptive norm constraint. For $d_c(\cdot)$ in this equation, it represents the measurement for neighboring pixels in τ different directions. An approximately rotationally symmetric operator within a 3×3 grid has proved to be a good choice for $d_c(\cdot)$ (Pan and Reeves 2006, Shen and Zhang 2009), as shown in Figure 3. Therefore, finite-difference approximations to second-order derivatives in four directions are employed. To define the data roughness, the measurement at pixel i of the data vector $\boldsymbol{u}$ ($HN_1HN_2 \times 1$) is given as

$$\begin{aligned} d_c^1(u_i) &= u_{i-1} - 2u_i + u_{i+1} \\ d_c^2(u_i) &= u_{i-HN_1} - 2u_i + u_{i+HN_1} \\ d_c^3(u_i) &= \frac{1}{2}(u_{i-HN_1-1} - 2u_i + u_{i+HN_1+1}) \\ d_c^4(u_i) &= \frac{1}{2}(u_{i+HN_1-1} - 2u_i + u_{i-HN_1+1}) \end{aligned} \tag{10}$$

We define the L_p norm as a constraint function, which satisfies some geometric properties. A common criticism of the L_2 norm–based regularization methods is that the sharp edges and detailed information in the estimates tend to be overly smoothed.

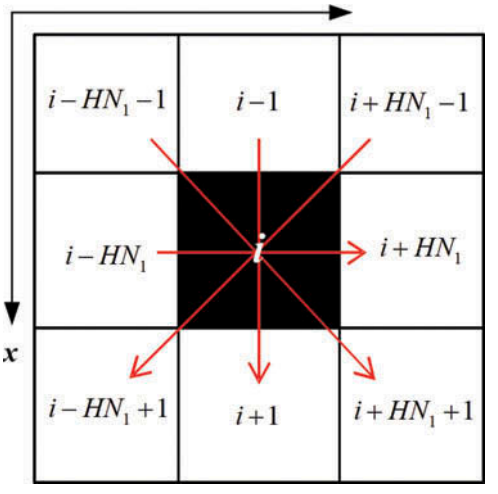

Figure 3. The structure of the symmetric operator (3 × 3) for MRF regularization for data with a size of $HN_1 \times HN_2$.

However, the L_2 norm is usually better in suppressing noise and overcoming the staircase effect than the L_1 norm (Bertaccini *et al.* 2012). The compromise here is to choose different constraint norms depending on the spatial distribution. Based on this, the problem is how to determine the constraint function used. The height change in DEM values can be dramatic, and often ranges from nearly zero or even negative to hundreds or thousands of meters in one dataset. Local gridded elevation changes vary with the terrain, as well as the sampling scale. Therefore, image gradients such as first- and second-order gradients are not suitable for describing the real hypsography of the earth's surface, because it would cause the threshold selection to be a tough task. In this paper, we use slope information for DEMs to distinguish different terrain features, and thus determine the constraint norm used in Equation (9). To adaptively select the threshold T_s, after calculating the slope $\boldsymbol{S}$ of $\boldsymbol{u}$ by Equation (6), we normalize $\boldsymbol{S}$ and choose the median value as the threshold in general cases. Therefore, the constraint norm for the pixel i is chosen as

$$p_i = \begin{cases} 2 & S_i < T_s \\ 1 & S_i \geq T_s \end{cases} \tag{11}$$

The universal objective function can be finally expressed as

$$\hat{\boldsymbol{u}} = \arg\min \left[\sum_k w_k \cdot \| (\boldsymbol{y}_k - \boldsymbol{A}_k u) \|_1^1 + \lambda \sum_i \sum_{t=1}^{\tau} \left\| d_c^t(u_i) \right\|_{p_i}^{p_i} \right] \tag{12}$$

with w_k, $d_c^t(\cdot)$, and p_i defined above. This is a hybrid-norm and nonlinear minimization problem. Using the iteratively reweighted norm proposed by Rodriguez and Wohlberg (2009), it can be efficiently solved by approximating the equation with a weighted L_2 norm, whose convergent properties have been provided. The preconditioned conjugate

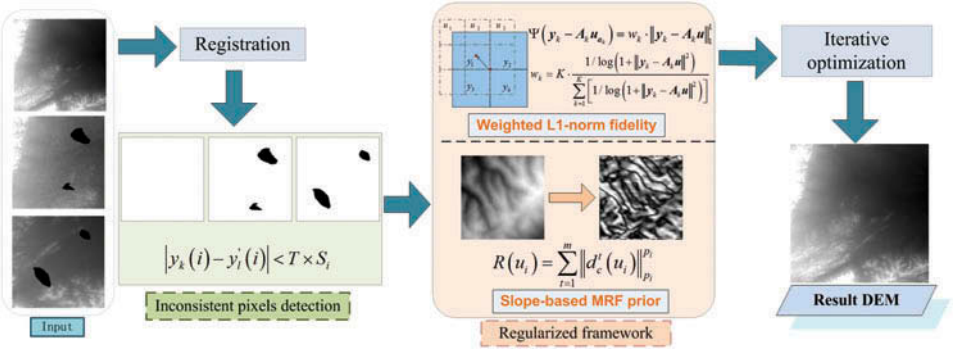

Figure 4. The flowchart for the proposed algorithm.

gradient (PCG) method (Ng *et al*. 2007b) is then utilized to iteratively optimize the energy function after linearization. More detailed information can be found in previous work (Yue *et al*. 2014). The flowchart for the proposed regularized algorithm is given in Figure 4.

3. Experiments and discussions

The experiments consisted of two parts, to verify the proposed method under synthetic and real cases, respectively. DEM products with various scales and characteristics were used, while different terrain features were also considered to test the performance and robustness of the proposed method.

3.1. Experiment data

3.1.1. CGIAR-CSI SRTM v4.1

The SRTM data were collected over an 11-day mission in 2000, with the elevations measured via radar interferometry using an onboard/outboard antenna system and single-pass data acquisition (Farr and Kobrick 2000). The resolution of this product was 3 arc (~90 m) on the WGS84 coordinate. The current version of this DEM product was released by the Consortium for Spatial Information of the Consultative Group of International Agricultural Research (CGIAR-CSI) after data improvement and void filling. It covered about 80% of the globe (from 60°N to 60°S) (Jarvis *et al*. 2008). The dataset was regarded as the most quality-controlled and one of the broadest coverage DEMs currently available.

3.1.2. ASTER GDEM2

The ASTER mission was a joint project between NASA and the Ministry of Economy, Trade and industry (METI), and the elevation products were measured onboard NASA's Terra satellite since 2000 (Tachikawa *et al*. 2011). The current version released in 2011 was the second data product after resolution improvement and water body coverage refinement, with a resolution of 1 arc (~30 m) on the WGS84 coordinate. It covered a nearly global geographic extent (latitudes from 83°S to 83°N). However, the dataset was known to be influenced by a variety of artifacts and anomalies that limit its immediate

use. With elevation measured from the earth's reflective surface, the accuracy of ASTER GDEM2 was sensitive to land cover, such as forest canopies and buildings. Furthermore, numerous voids at high latitudes (above 60°N) and low latitudes (below 60°S) were also problems (Wang *et al*. 2011, Robinson *et al*. 2014).

3.1.3. *WorldDEM*

This dataset was a new product that was first made available in 2014. WorldDEM was the product of the TanDEM-X Mission (TerraSAR-X add-on for digital elevation measurements), realized as a Public–Private Partnership between Airbus Defence and Space (ADS) and the German Aerospace Center (DLR). According to the product report released by ADS (Airbus Defence and Space 2014), the resolution of this DEM product was about 12 m on the WGS84 coordinate, with an absolute vertical accuracy of 4 m, which was much higher than any other global satellite-based elevation model available. The dataset has not been released globally and for free so far, but it was possible to download sample data for South Australia for academic research. A simple comparison of the three global elevation data products is given in Figure 5. This was a small area in Quorn, Australia, with relatively smooth relief. We can see that the WorldDEM data give the most attractive visual effect.

3.1.4. *Air-borne INSAR data*

The final dataset we used was the C-band TOPSAR interferometric 10 m DEM, which was derived from air-borne C-band INSAR data from the NASA/Jet Propulsion Laboratory (JPL) TOPSAR instrument (Chen *et al*. 2009). It was collected in 1998 near Camp Roberts, California, United States. The C-band INSAR-derived 10 m DEM has been reported that the vertical accuracy has also been widely verified by the root mean

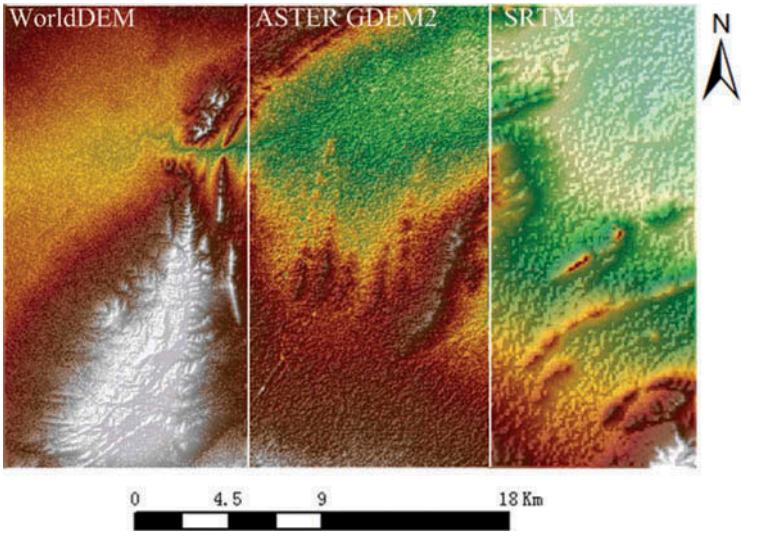

Figure 5. Comparison of the three DEM products. From left to right: 12 m WorldDEM, 30 m ASTER GDEM2, and 90 m SRTM.

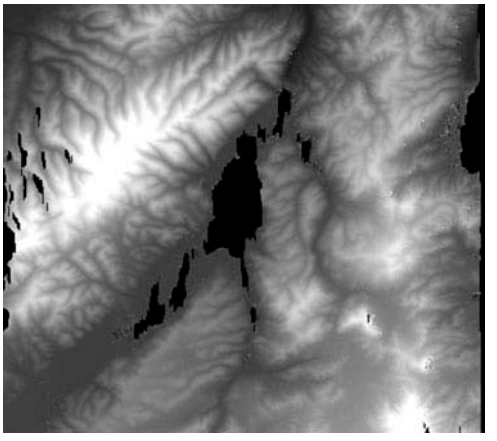

Figure 6. The partial C-band InSAR-derived 10 m DEM. Large-area data voids and missing values can be observed.

square deviation (RMSD) as being less than 7 m over large areas, on a local coordinate system (Schuler *et al*. 1998). Despite the considerable spatial resolution and vertical accuracy, the limited spatial coverage and the data voids were the main obstacles for its further application. We give a sample area of this dataset in Figure 6, with obvious data voids in the area.

3.2. Synthetic experiments

In this part, we conducted two sets of synthetic experiments to test and quantitatively evaluate the efficacy of the proposed method. In the two experiments, WorldDEM data with a small selected area (192 × 192) were used as the original data, as well as the reference data for quantitative evaluation. The height values range from 377.22 to 795.82 m. Following the generative model in Equation (2), we created three data with different scales, coverage, and noise levels in each experiment. According to the previous research (Fisher and Tate 2006, Gallant 2011), we defined the noise in the DEM as random noise satisfying a Gaussian distribution.

From the point of view of terrain analysis, the representative ability of the morphological and hydrological features of DEMs is also critical. As we know, channel networks are significant skeleton information in the description of terrain surfaces (Lashermes *et al*. 2007, Passalacqua *et al*. 2010). To measure the reliability of the reconstructed result in a hydrographic application, channel networks in the region were extracted for evaluation. In addition, as a fundamental element of a topographic map, we took contour lines generated from the reconstructed results as one of the better ways of visual evaluation of the fusion result.

The first experiment was under a noiseless condition, which means that no simulated noise was added in the degradation process. The resolutions of the three acquired DEM datasets were 12 m, 20 m, and 30 m, respectively (Figure 7). Using the three datasets with a size of 76 × 76, our purpose was to reconstruct seamless DEM data (192 × 192) with a 12 m resolution, and the same coverage as the 30 m DEM, by fusing the supplementary information between them. The fused result by the proposed method was compared with the

Figure 7. The simulated data used in the first synthetic experiment. (a–c) The DEM data with resolutions of 30 m, 20 m, and 12 m, respectively, while their coverage areas decrease.

interpolated results for the 30 m data by the bilinear, IDW, spline, and kriging interpolation methods, which are commonly used in DEM densification. In addition, considering the input HR information, mosaic results integrating the complementary data are also given for a fair comparison. The quantitative indexes of the root mean square error (RMSE) (Chen and Li 2013) and mean absolute error (MAE) were used to evaluate the vertical accuracy of the results. As in Equation (13), $\mathbf{u}$ represents the reconstructed measurement, while $\mathbf{u}_{\text{ref}}$ is the reference data of Ω points. The visual results can display the continuous property of the reconstructed data. For more detailed analysis, the maximum and minimum values in the results were also presented in Tables 1 and 2, respectively.

$$\begin{aligned} \text{RMSE} &= \sqrt{\frac{\sum (u - u_{\text{ref}})^2}{\Omega}} \\ \text{MAE} &= \frac{\sum |\boldsymbol{u} - \boldsymbol{u}_{\text{ref}}|}{\Omega} \end{aligned} \tag{13}$$

Table 1. The quantitative results for the first experiment.

	Bilinear	IDW	Spline	Kriging	Mosaic	Proposed
MAE (m)	3.3637	2.1752	1.6131	1.6847	0.9261	0.6373
RMSE (m)	4.2042	2.7942	1.9778	2.0810	1.3548	0.8138
ΔMAX (m)	13.2254	13.2448	10.2128	11.0408	10.3896	8.9377
ΔMIN (m)	−18.0399	−13.3466	−11.0835	−11.1600	−10.4210	−10.2900

Note: Δ, difference between the corresponding result and reference.

Table 2. The quantitative results for the second experiment.

	Bilinear	IDW	Spline	Kriging	Mosaic	MVF	Proposed
MAE (m)	4.2521	3.1695	3.7236	3.6092	13.1435	2.8566	1.9263
RMSE (m)	5.3514	4.0247	4.6803	4.6359	80.9160	3.9431	2.5801
ΔMAX (m)	22.4949	17.8302	21.0339	22.8430	28.0336	28.0336	13.6748
ΔMIN (m)	−20.6136	−16.2014	−15.9914	−24.3264	−776.1406	−24.5125	−16.7612

Note: Δ, difference between the corresponding result and reference.

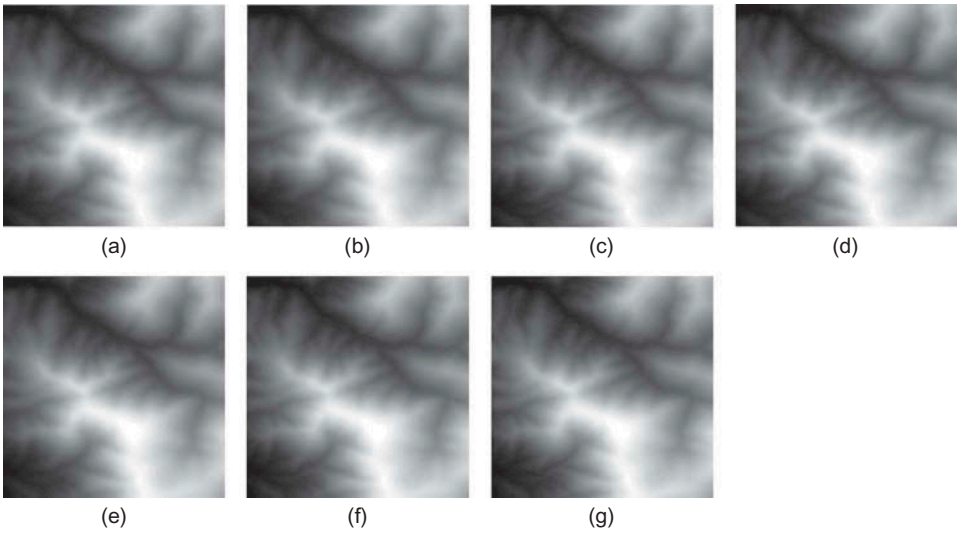

Figure 8. The reconstruction results for the first experiment. (a–d) The results for the bilinear, IDW, spline, and kriging interpolation methods; (e, f) the results reconstructed by mosaic and the proposed method. The original reference data are shown in (g).

The reconstruction results are shown in Figure 8, as well as the referenced data. From Figure 8, it can be seen that the bilinear and IDW interpolation methods obtain the most unsatisfactory results, with an obvious smooth terrain surface apparent in the upper right and middle part. The kriging and spline methods perform better at preserving the detailed features; however, the limited information makes these methods difficult for handling more complex terrains. The main objective in this experiment was to test the performance under an ideal situation. There is a narrow span in the data resolution, and no noise affects the consistency between the data in this case. Therefore, the mosaic method can acquire a relatively fine result. However, in the upper right and the lower left corner in Figure 8(e) and 8(f), we can see that compared with the mosaic result, the proposed method can reconstruct a seamless enhanced elevation result, rather than a simple data integration. There are sharp edges and features in the areas even without input high-resolution details, as shown in Figure 8(f). The quantitative results in Table 1 also confirm the tendency. Only the proposed method can reconstruct the topographic relief well.

However, the ideal case in the first experiment cannot practically describe general situations. The second experiment was therefore simulated as closer to a real case. Despite the down-sampling and coverage offset, noise and data voids were considered. The same operations were conducted as in the first experiment to get the three DEM datasets. We then added zero mean Gaussian noise with a standard deviation (SD) of 5 in the 20 m resolution data, and noise with SD 8 in the 30 m resolution data. Arbitrary missing values were simulated in the 12 m resolution DEM. The input data in this experiment are shown in Figure 9.

As mentioned in Section 2, by the use of the regularized framework proposed in this paper, we can simultaneously handle data fusion, noise suppression, and void filling. The results for this case are displayed in Figure 10. In this group, we use a color map generated from the reconstructed DEM data to display the results for better visual

Figure 9. The simulated data used in the second synthetic experiment. (a–c) The DEM data with resolutions of 30 m, 20 m, and 12 m, respectively, with different noise levels and data voids.

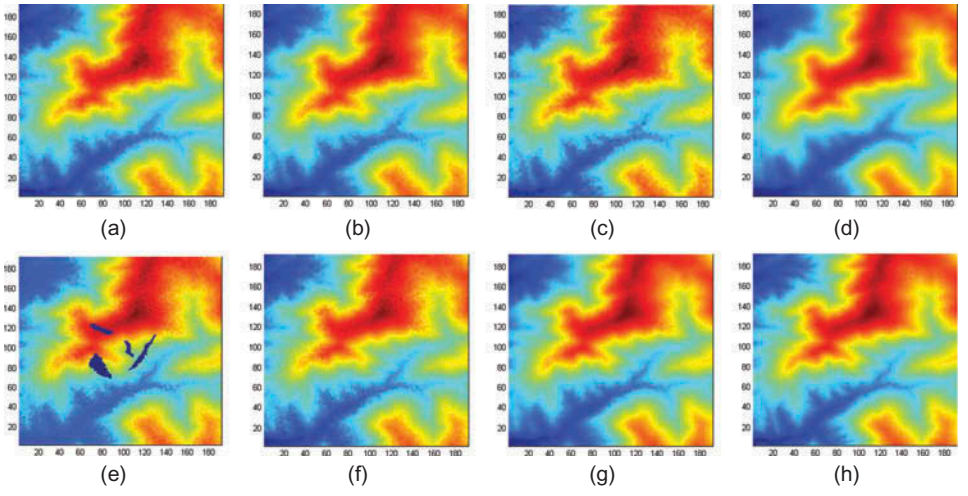

Figure 10. The reconstruction results for the second experiment. (a–d) The results for the bilinear, IDW, spline, and kriging interpolation methods, and (e, f) the results reconstructed by mosaic, and the mosaic result after void filling (MVF). (g) Result of the proposed method, and the original reference data are shown in (h).

interpretation. It can be seen that with noise, the advantages of the proposed method are more prominent. All the interpolation methods have difficulty in achieving a balance between suppressing noises and preserving details. The kriging method can overcome the effect of noise to a certain extent, but it simultaneously smoothes the sharp terrain features. Because there are voids existing, we utilized the kriging method to fill the voids in the mosaic result as postprocessing, and obtained an acceptable result. In this paper, we use 'MVF' to indicate the mosaic result with a void-filling process.

Under this complex case, only the proposed method can obtain a similar result to the reference data, considering the inconsistency between the input data. In this case, the weights were assigned as in Equation (8), in accordance with the quality of the input data. Thus, the 12 m data got the highest weight, while the noisy 30 m DEM data made the smallest contribution to the reconstructed result. The elevation deviation between the comparative

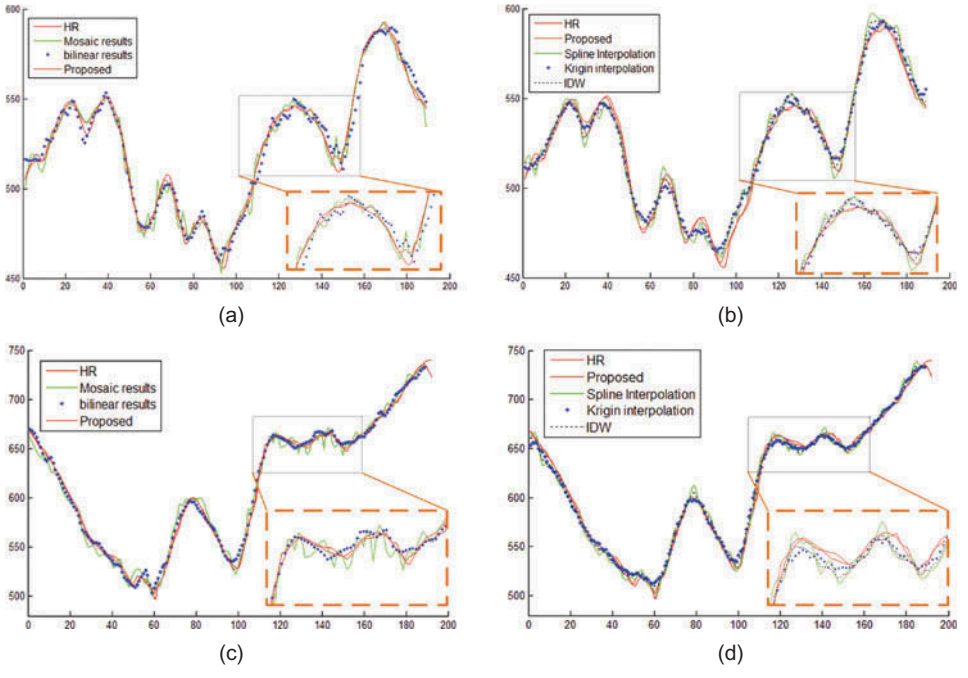

Figure 11. The horizontal and vertical elevation profiles for the comparative results in the second synthetic experiment. (a, b) The horizontal profile, and (c, d) the vertical elevation profile.

methods and the proposed method can be clearly observed in the horizontal and vertical elevation profiles, as shown in Figure 11. The result of the proposed method, displayed as the red line, closely resembles the reference data, in both directions. Although the kriging method can get a visually fine result with the small voids in this test, it can be observed that the height values are indeed estimated unfaithfully. The quantitative assessment in Table 2 also shows the clear superiority of the proposed method. Interpolation methods were inevitably under the influence of noises, thus the height values in the corresponding result will be somewhat higher than the referenced data. IDW method achieved the best quantitative index among the interpolation methods, probably for the preservation of sharp details. Nevertheless, terrain noises inevitably affect the accuracy. The proposed method performs best by combining SR, noise suppression, and void filling into a universal framework.

Furthermore, we used the results acquired by kriging interpolation, MVF, and the proposed method to extract the channel network, as shown in Figure 12. This procedure was undertaken by the hydrology analysis tool and map algebra tool in ArcGIS software, following the steps of filling sinks, tracing flow directions, computing the flow accumulation, and conditional operation. It can be observed in Figure 12 that the channel network generated from the proposed method closely resembles the reference data. The results show that the channel network in Figure 12(a) and 12(b) has too many spurious branches while missing some significant branches in the bottom part. This is caused by the noise and subtle distortions in the DEM terrain representation. With noise, the mosaic results preserve the inconsistency between the data, and thus there is an apparent staircase effect.

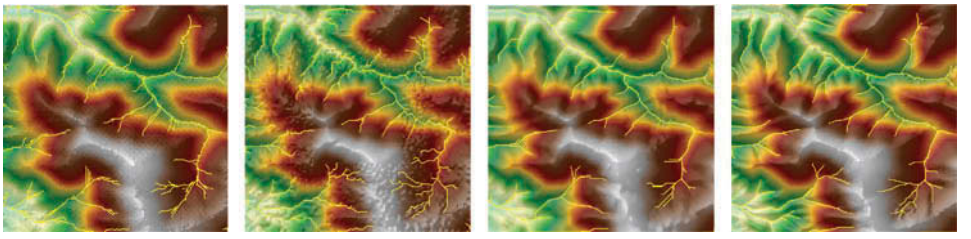

Figure 12. The extracted channel network in the second experiment. (a–c) The extraction results from the DEM data reconstructed by kriging interpolation, MVF, and the proposed method, respectively. (d) The reference data.

3.3. *Real data experiments*

We also conducted three sets of experiments using real DEM data, with the DEM products described in Section 3.1 being involved in the test. In the three tests, there might not be ideal referenced data for evaluation. Fortunately, the subjective visual effects can help us judge the methods' performance. For the first real data experiment, the proposed method was tested for the fusion of 12 m WorldDEM data and 30 m resolution ASTER GDEM data with a relatively small selected area (181 × 181). The input data were from Quorn, Australia, which belong to a relatively diverse terrain, with the elevation ranging from 118 to 666 m. The results (452 × 452) are given in Figure 13. In this case, the main problem was the noise existing in the GDEM data; however, the proposed method is good at handling such a problem.

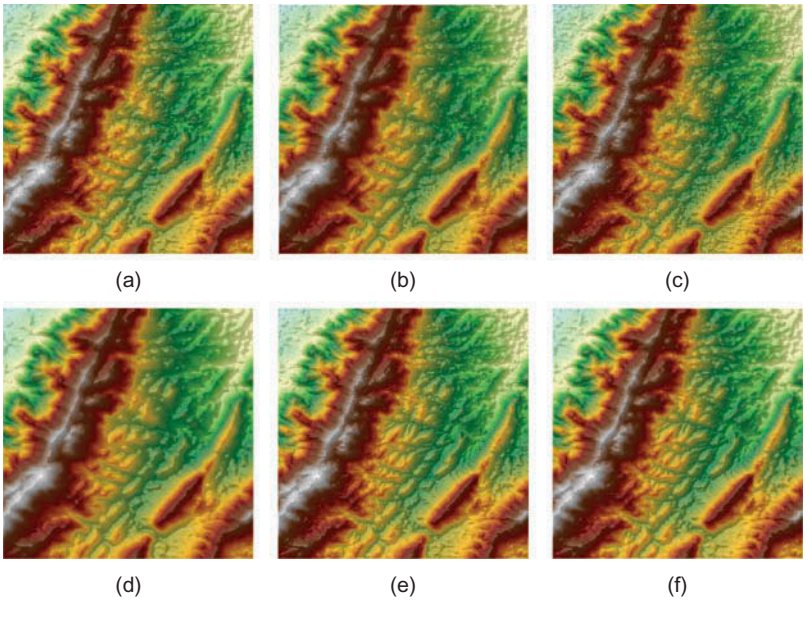

Figure 13. The reconstructed results in the first real data experiment. (a–d) The results for the bilinear, IDW, spline, and kriging interpolation methods, and (e, f) the results reconstructed by mosaic and the proposed method.

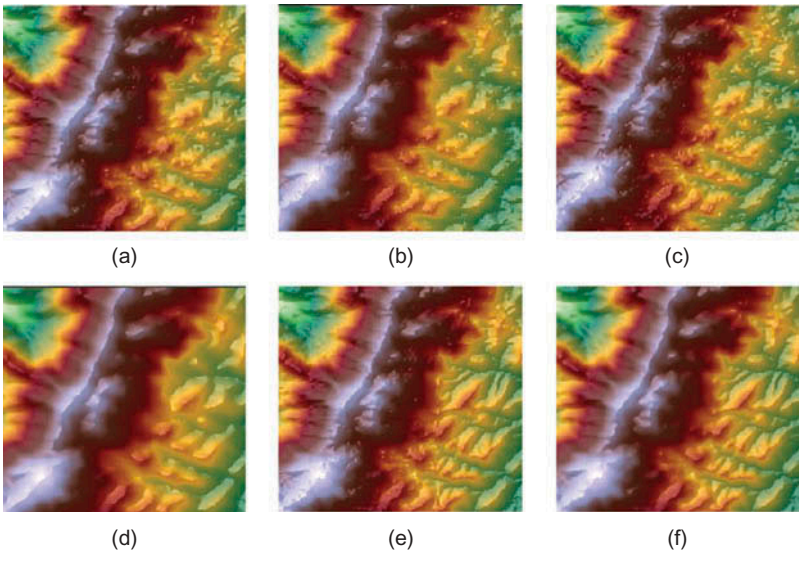

Figure 14. Detailed regions cropped from Figure 13(a–f).

In Figure 13, we can see that the results in parts (a)–(c) are severely influenced by noise. It is worth mentioning that the subtle rolling topography, for example, the upper right part of the figures, does not represent real terrain. This is in fact caused by noise, which is a common problem in GDEM data. Among the interpolation methods, the kriging algorithm is able to suppress the noise by tuning the statistical parameters. However, compared with the result of the proposed method, the kriging result loses the sharp features, while the mosaic result suffers from noise and the artifacts near the mosaic edges. To allow a better visual judgment, cropped regions from Figure 13(a)–(f) are given in Figure 14(a)–(f). Compared with the results of the other methods, the result of the proposed method not only removes the noise but also fuses the HR and LR information to be oversampled DEM data without apparent joints.

The objective of the second real data experiment was to fuse an air-borne SAR dataset with a space-borne elevation data product. Given that air-borne SAR data are often acquired at a high cost and are limited to relatively narrow areas, we tried to improve the quality of the HR dataset by fusing it with other auxiliary datasets by the use of the proposed method. The kriging interpolation method was used for comparison, as well as the mosaic method. The C-band InSAR-derived 10 m DEM we used in this paper was introduced in Section 3.1.4. In this experiment, we selected an area with a size of 300 × 300 (Figure 15), and attempted to obtain a 900 × 900 DEM with the same coverage as the 30 m data. Differing from the experiments before, the considerable inconsistency between the two kinds of data makes the problem more complex. First, the coordinate systems need to be matched before the fusion. Errors brought about by the coordinate registration may affect the accuracy of the result. Second, the different vertical coordinate systems of the two datasets should also be considered. In addition, voids with a large area exist in the data. For the first problem, the scale-invariant feature transform (SIFT) algorithm was utilized for the registration, and a manual check was implemented to reject the errors. By tuning the regularization parameter, the proposed method can make use of the robustness of the L_1 norm to overcome the registration errors. In terms of the second

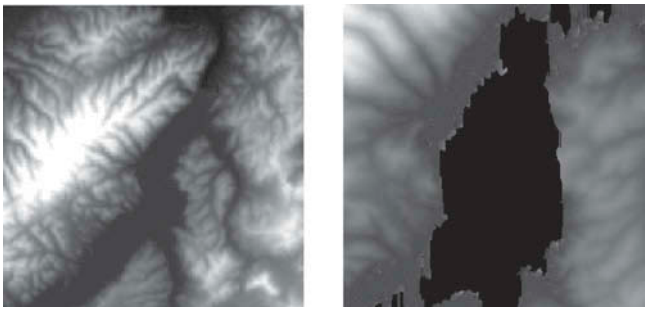

Figure 15. The input multi-scale DEM data in the second real experiment. (a) 30 m GDEM data, and (b) C-band InSAR-derived 10 m DEM with large-area voids as input data.

problem, to ensure the consistency of the vertical coordinate systems, we chose a small shared area in the input data after registration to calculate the average vertical offsets between them. The offset values were then regarded as the vertical differences between the input data on different datum.

According to the results given in Figure 16, the proposed method can obtain an acceptable result with large areas of missing values. In Figure 16, we give the complete reconstructed result by the proposed method in Figure 16(a), with the generated contour lines. Figure 16(b)–(e) are the cropped regions corresponding to the rectangular area in Figure 16(a) processed by the different methods. It can be observed that with a large missing area, the mosaic method cannot handle this situation, even when further processed by kriging interpolation. Compared with the result of the interpolation method, the

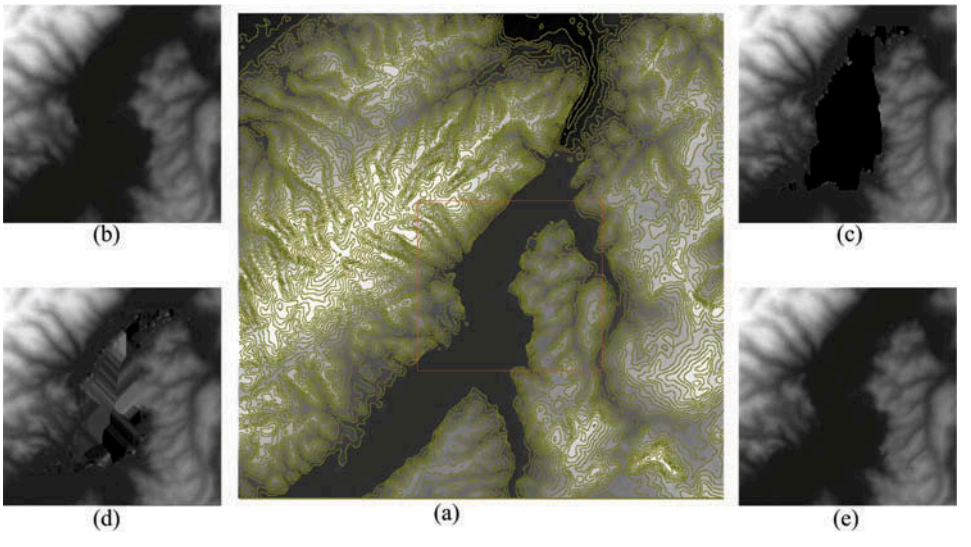

Figure 16. The reconstructed results in the second real data experiment. (a) Complete result and generated contour lines for the proposed method. (b–e) The cropped regions for kriging interpolation, the mosaic method, MVF, and the proposed method ($T = 50$), respectively.

Figure 17. The reference L-band PolSAR Pauli color-coded image (|HH + VV|, blue; |HH − VV|, red; 2|HV| green).

proposed method can use the auxiliary information obtained from the multi-scale DEM data, and thus obtain more accurate and detailed terrain features. To better evaluate the results, we give the L-band PolSAR Pauli color-coded image with a 10 m resolution as the reference in Figure 17. It can be clearly observed that results of the proposed method can provide a more accurate bank line, which makes sense in hydrological applications. The contours generated from Figure 16(b)–(e), respectively, are given in Figure 18. The details are enhanced by fusing the high-resolution DEM data, while the data voids are filled with the supplementary information in the LR data by the proposed method. The proposed method consistently obtains more visually attractive contour line results and detailed terrain features, especially in the two highlighted regions.

For better comparison and parameter analysis, we also give the results with the detection method expressed in Equation (4). As Figure 19 shows, without spatially adaptive strategy, we cannot distinguish details and noises in the flat regions (e.g., the water area). And the inaccurate detection results will result in the remaining anomalies in the fused data. The adaptive method employs slope information to increase the accuracy of anomalies detection and exclusion in the fusion.

The last real data experiment was the fusion of three multi-scale DEM datasets. In this experiment, in addition to the C-band InSAR-derived 10 m DEM and the 30 m GDEM data, we also took 90 m SRTM DEM data as auxiliary input data. Here, the resolution gap between the 10 m data and the 90 m data becomes the main critical issue. We need to reconstruct a DEM with a size of 720 × 720 by fusing three small areas of data (80 × 80). However, the well-controlled quality of the SRTM data makes the result visually attractive. The color maps covered by the generated contour lines are shown in Figure 20, while partial comparative results are given in Figure 21. It can be seen that there are obvious visual differences in this group of results. Overall, the proposed method provides more continuous and detail-enhanced large-scale DEM data with a 10 m resolution.

4. Discussion and conclusion

Although a variety of DEM products were available, they were all characterized by trade-offs in spatial coverage, data resolution, and quality. In general, DEMs with a very high spatial resolution (less than 30 m) were usually limited to a narrow coverage and have

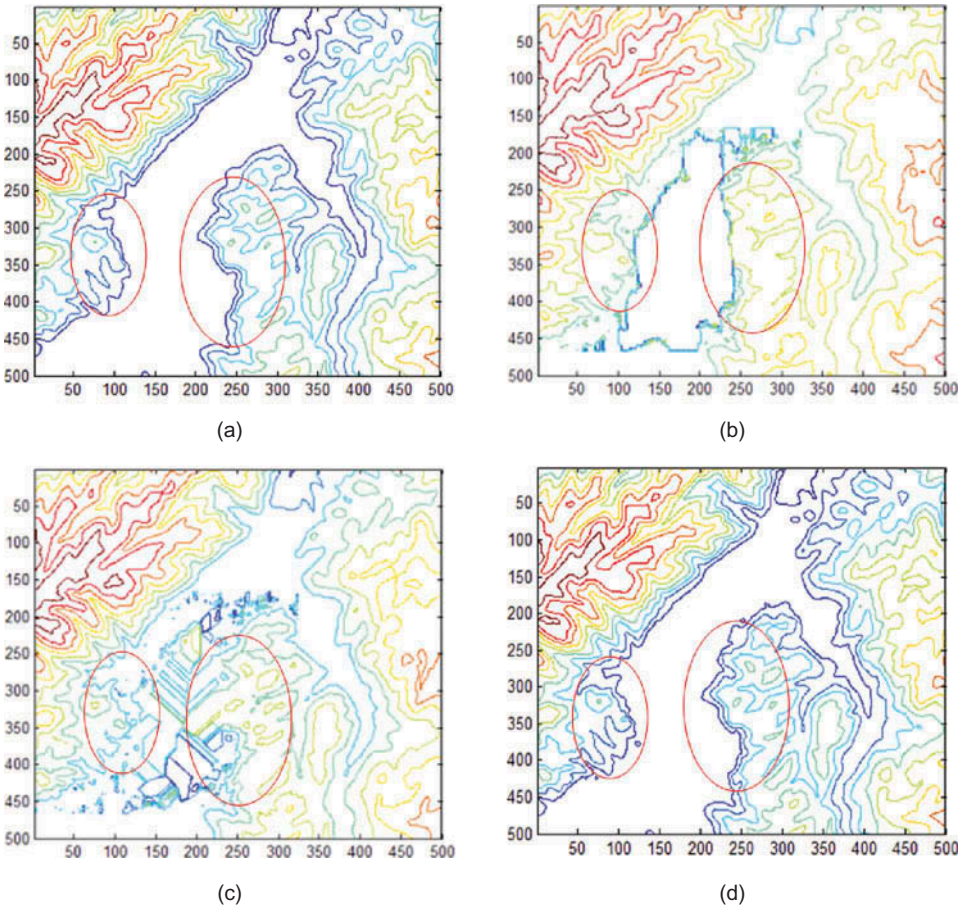

Figure 18. The comparative generated contour lines for the results in the second real data experiment. (a–d) The results for the kriging interpolation, the mosaic method, MVF, and the proposed method, respectively.

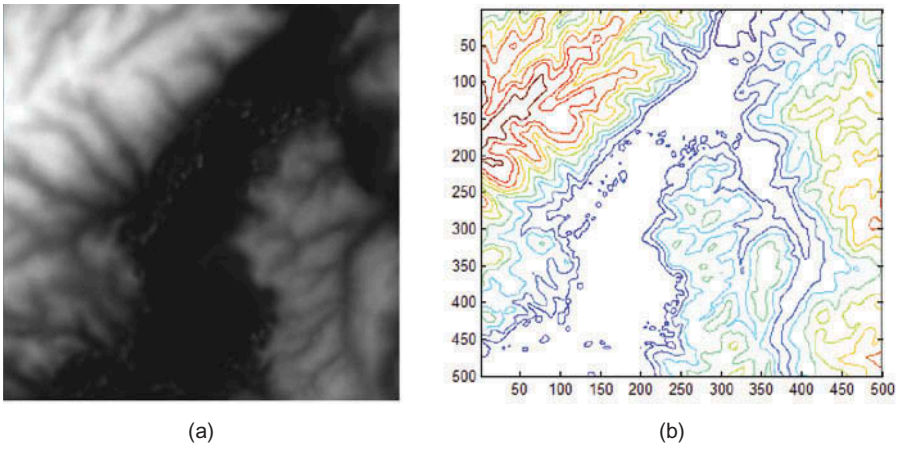

Figure 19. The comparative results with anomalies detection by (Equation (4)) with $T = 45$. (a, b) The partial fused data and corresponding generated contours in the second real data experiment, respectively.

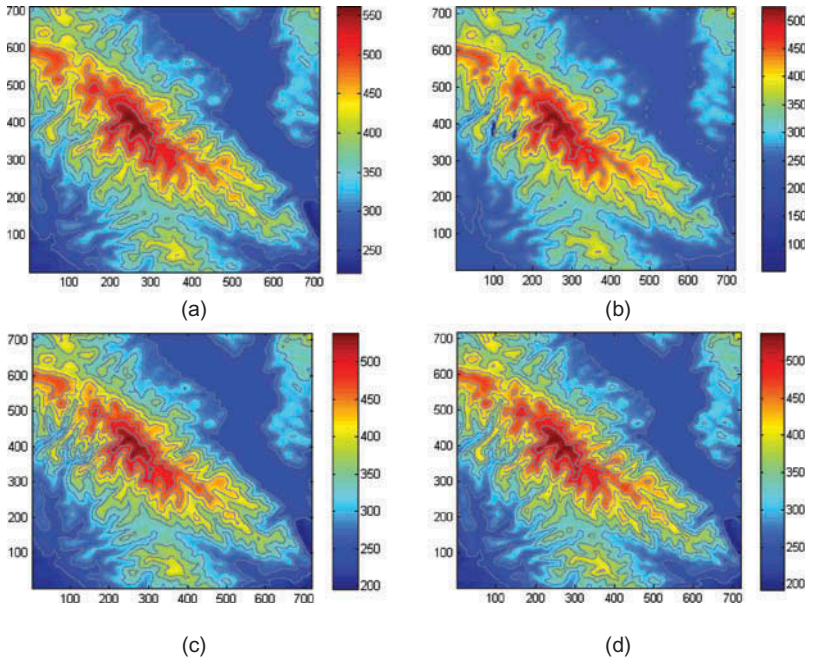

Figure 20. The corresponding color maps covered by the generated contour lines in the last experiment. (a–d) The results for kriging interpolation, the mosaic method, the MVF, and the proposed method, respectively.

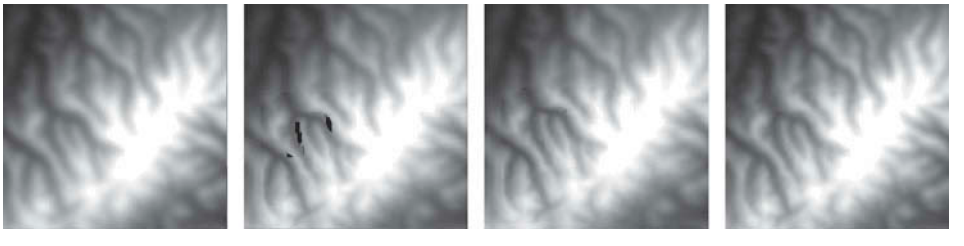

Figure 21. The partially reconstructed results in the third real data experiment. (a–d) The results for kriging interpolation, the mosaic method, the MVF, and the proposed method, respectively.

data quality problems (e.g., data voids and noise). Therefore, in this paper, we have proposed a novel regularized framework for multi-scale DEM fusion. Rather than a simple mosaic result of data with different spatial coverage, the reconstructed data were generated using the supplementary information between different DEMs. In the proposed method, a weighted L_1 norm was utilized to restrain the errors brought about by horizontal errors, while a slope-based spatially adaptive MRF prior was employed for the spatial constraint. Multiple problems, including data inconsistency, noise, and data voids can be overcome by taking advantage of the proposed method.

The experimental results confirmed the performance of the proposed method in various cases, compared with other methods, including popular geo-statistical

interpolation algorithms and a mosaic method. We conducted two synthetic experiments to test the performance under simulated conditions. It can be seen that the proposed method obtained more satisfactory results in these two experiments by both quantitative and visual evaluation. However, real cases are more complex. In the fusion of the famous global DEM products and air-borne SAR-derived DEM data, the proposed method proved its effectiveness and robustness to the significant changes between data from multiple sources, and even with large resolution gaps.

The main purpose in this paper was to propose a new method to deal with the integration of DEMs. However, there were still some limitations to the proposed method. In this paper, the model took the main factors such as the scaling effect, datum differences, random noise, and horizontal or vertical errors among multi-scale DEM products into consideration. However, more complex problems such as other unpredictable production errors and the effect of cartographic generalization were not included in the proposed method. In our future work, more possible degradation factors will be taken into account to improve the accuracy of the fused DEM data. Besides, the accelerated strategies are desired for large-scale DEM fusion.

Acknowledgements

The authors thank the editors and the anonymous reviewers for their valuable suggestions. They also thank Dr Xianwei Zheng and Dr Lei Shi for their help with data preparation in this work.

Disclosure statement

No potential conflict of interest was reported by the authors.

Funding

This research is supported by the National Natural Science Foundation of China [grant number 41422108], [grant number 41401383]; Wuhan Science and Technology Program [grant number 2013072304010825]; Program for Changjiang Scholars and Innovative Research Team in University [grant number IRT1278].

References

Airbus Defence and Space, 2014. *WorldDEM: the new standard of global elevation models* [online.] Available from: http://www2.astrium-geo.com/files/pmedia/public/r5434_9_geo_022_worlddem_en_low.pdf [Accessed 22 May 2014].

Bertaccini, D., *et al*., 2012. An adaptive norm algorithm for image restoration. *In*: *Third international conference, SSVM 2011*, Ein-Gedi, Israel. Berlin: Springer, 194–205.

Bulyshev, A., *et al*., 2011. A super-resolution algorithm for enhancement of FLASH LIDAR data. *In*: *IS&T/SPIE electronic imaging*. San Francisco, CA: International Society for Optics and Photonics, 78730F-78730F-78737.

Chaplot, V., *et al*., 2006. Accuracy of interpolation techniques for the derivation of digital elevation models in relation to landform types and data density. *Geomorphology*, 77 (1–2), 126–141. doi:10.1016/j.geomorph.2005.12.010

Chen, C. and Li, Y., 2013. An orthogonal least-square-based method for DEM generalization. *International Journal of Geographical Information Science*, 27 (1), 154–167. doi:10.1080/13658816.2012.674136

Chen, C. and Yue, T., 2010. A method of DEM construction and related error analysis. *Computers & Geosciences*, 36 (6), 717–725. doi:10.1016/j.cageo.2009.12.001

Chen, X., Wang, C., and Zhang, H., 2009. DEM generation combining SAR polarimetry and Shape-from-Shading techniques. *IEEE Geoscience and Remote Sensing Letters*, 6 (1), 28–32. doi:10.1109/LGRS.2008.2002810

Chen, Z., *et al*., 2013. DEM densification using perspective shape from shading through multi-spectral imagery. *IEEE Geoscience and Remote Sensing Letters*, 10 (1), 145–149. doi:10.1109/LGRS.2012.2195471

Darboux, F. and Huang, C.-H., 2003. An instantaneous-profile laser scanner to measure soil surface microtopography. *Soil Science Society of America Journal*, 67 (1), 92–99.

Erdogan, S., 2009. A comparison of interpolation methods for producing digital elevation models at the field scale. *Earth Surface Processes and Landforms*, 34 (3), 366–376. doi:10.1002/esp.v34:3

Farr, T.G. and Kobrick, M., 2000. Shuttle Radar Topography Mission produces a wealth of data. *EOS, Transactions American Geophysical Union*, 81 (48), 583–585.

Farsiu, S., *et al*., 2004. Fast and robust multiframe super resolution. *IEEE Transactions on Image Processing*, 13 (10), 1327–1344. doi:10.1109/TIP.2004.834669

Fisher, P.F. and Tate, N.J., 2006. Causes and consequences of error in digital elevation models. *Progress in Physical Geography*, 30 (4), 467–489. doi:10.1191/0309133306pp492ra

Fu, P. and Rich, P.M., 2002. A geometric solar radiation model with applications in agriculture and forestry. *Computers and Electronics in Agriculture*, 37 (1–3), 25–35. doi:10.1016/S0168-1699(02)00115-1

Gallant, J., 2011. Adaptive smoothing for noisy DEMs [online]. *In*: *Geomorphometry 2011*. Redlands, CA, 7–9. Available from: http://www.geomorphometry.org/ [Accessed 30 May 2011].

Hirano, A., Welch, R., and Lang, H., 2003. Mapping from ASTER stereo image data: DEM validation and accuracy assessment. *ISPRS Journal of Photogrammetry and Remote Sensing*, 57 (5–6), 356–370. doi:10.1016/S0924-2716(02)00164-8

Hormann, K., Spinello, S., and Schröder, P., 2003. C1-continuous terrain reconstruction from sparse contours. *In*: *VMV*. Munich: Aka GmbH, 289–297.

Huang, C., Chen, Y., and Wu, J., 2014. DEM-based modification of pixel-swapping algorithm for enhancing floodplain inundation mapping. *International Journal of Remote Sensing*, 35 (1), 365–381. doi:10.1080/01431161.2013.871084

Irani, M. and Peleg, S., 1991. Improving resolution by image registration. *CVGIP: Graphical Models and Image Processing*, 53 (3), 231–239. doi:10.1016/1049-9652(91)90045-L

Jarvis, A., *et al*., 2008. *Hole-filled seamless SRTM data V4* [online]. International Centre for Tropical Agriculture (CIAT). Avalaible from: http://srtm.csi.cgiar.org [Accessed 10 July 2007].

Jhee, H., *et al*., 2013. Multiscale quadtree model fusion with super-resolution for blocky artefact removal. *Remote Sensing Letters*, 4 (4), 325–334. doi:10.1080/2150704X.2012.729869

Jiang, H., *et al*., 2014. Fusion of high-resolution DEMs derived from COSMO-SkyMed and TerraSAR-X InSAR datasets. *Journal of Geodesy*, 88 (6), 587–599. doi:10.1007/s00190-014-0708-x

Joshi, M.V., Chaudhuri, S., and Panuganti, R., 2005. A learning-based method for image super-resolution from zoomed observations. *IEEE Transactions on Systems, Man and Cybernetics, Part B (Cybernetics)*, 35 (3), 527–537. doi:10.1109/TSMCB.2005.846647

Karkee, M., Steward, B.L., and Aziz, S.A., 2008. Improving quality of public domain digital elevation models through data fusion. *Biosystems Engineering*, 101 (3), 293–305. doi:10.1016/j.biosystemseng.2008.09.010

Kellndorfer, J., *et al*., 2004. Vegetation height estimation from shuttle radar topography mission and national elevation datasets. *Remote Sensing of Environment*, 93 (3), 339–358. doi:10.1016/j.rse.2004.07.017

Lashermes, B., Foufoula-Georgiou, E., and Dietrich, W.E., 2007. Channel network extraction from high resolution topography using wavelets. *Geophysical Research Letters*, 34, L23S04. doi:10.1029/2007GL031140

Li, S.Z. and Singh, S., 2009. *Markov random field modeling in image analysis*. London: Springer Science & Business Media.

Liu, X., 2008. Airborne LiDAR for DEM generation: some critical issues. *Progress in Physical Geography*, 32 (1), 31–49. doi:10.1177/0309133308089496

Ng, M.K., *et al*., 2007a. Zoom-based super-resolution reconstruction approach using prior total variation. *Optical Engineering*, 46 (12), 127003-127003-127011.

Ng, M.K., *et al*., 2007b. A total variation regularization based super-resolution reconstruction algorithm for digital video. *Eurasip Journal on Advances in Signal Processing*, 2007, 1–17. doi:10.1155/2007/74585

Pan, R. and Reeves, S.J., 2006. Efficient Huber–Markov edge-preserving image restoration. *IEEE Transactions on Image Processing*, 15 (12), 3728–3735. doi:10.1109/TIP.2006.881971

Park, S.C., Park, M.K., and Kang, M.G., 2003. Super-resolution image reconstruction: a technical overview. *IEEE Signal Processing Magazine*, 20 (3), 21–36. doi:10.1109/MSP.2003.1203207

Passalacqua, P., *et al*., 2010. A geometric framework for channel network extraction from lidar: Nonlinear diffusion and geodesic paths. *Journal of Geophysical Research: Earth Surface (2003–2012)*, 115 (F1). doi:10.1029/2009JF001254

Reuter, H.I., Nelson, A., and Jarvis, A., 2007. An evaluation of void-filling interpolation methods for SRTM data. *International Journal of Geographical Information Science*, 21 (9), 983–1008. doi:10.1080/13658810601169899

Robinson, N., Regetz, J., and Guralnick, R.P., 2014. EarthEnv-DEM90: A nearly-global, void-free, multi-scale smoothed, 90m digital elevation model from fused ASTER and SRTM data. *ISPRS Journal of Photogrammetry and Remote Sensing*, 87, 57–67. doi:10.1016/j.isprsjprs.2013.11.002

Rodriguez, P. and Wohlberg, B., 2009. Efficient minimization method for a generalized total variation functional. *IEEE Transactions on Image Processing*, 18 (2), 322–332. doi:10.1109/TIP.2008.2008420

Schuler, D.L., *et al*., 1998. Topographic mapping using polarimetric SAR data. *International Journal of Remote Sensing*, 19 (1), 141–160. doi:10.1080/014311698216477

Shen, H. and Zhang, L., 2009. A MAP-based algorithm for descripting and imprinting of remotely sensed images. *IEEE Transactions on Geoscience and Remote Sensing*, 47 (5), 1492–1502. doi:10.1109/TGRS.2008.2005780

Song, H., *et al*., 2015. Improving the spatial resolution of landsat TM/ETM+ through fusion with SPOT5 images via learning-based super-resolution. *IEEE Transactions Ongeoscience and Remote Sensing*, 53 (3), 1195–1204. doi:10.1109/TGRS.2014.2335818

Tachikawa, T., *et al*., 2011. *ASTER global digital elevation model version 2 – summary of validation results* [online]. Available from: http://www.jspacesystems.or.jp/library/archives/ersdac/GDEM/ver2Validation/Summary_GDEM2_validation_report_final.pdf [Accessed 31 August 2011].

Tian, Y. and Yap, K.-H., 2013. Joint image registration and super-resolution from low-resolution images with zooming motion. *IEEE Transactions on Circuits and Systems for Video Technology*, 23 (7), 1224–1234. doi:10.1109/TCSVT.2013.2242593

Tsai, R.Y. and Huang, T.S., 1984. Multi-frame image restoration and registration. *Advances in Computer Vision and Image Processing*, 1 (2), 317–339.

Wang, L., *et al*., 2011. Difference analysis of SRTM C-Band DEM and ASTER GDEM for global land cover mapping. *In*: *International symposium on image and data fusion (ISIDF)*. Tengchong, Yunnan: IEEE, 1–4.

Wechsler, S., 2007. Uncertainties associated with digital elevation models for hydrologic applications: a review. *Hydrology and Earth System Sciences Discussions*, 11 (4), 1481–1500. doi:10.5194/hess-11-1481-2007

Yue, L., *et al*., 2014. A locally adaptive L1−L2 norm for multi-frame super-resolution of images with mixed noise and outliers. *Signal Processing*, 105, 156–174. doi:10.1016/j.sigpro.2014.04.031

Zeng, X. and Yang, L., 2013. A robust multiframe super-resolution algorithm based on half-quadratic estimation with modified BTV regularization. *Digital Signal Processing*, 23 (1), 98–109. doi:10.1016/j.dsp.2012.06.013

Zhang, L., *et al*., 2012. Adjustable model-based fusion method for multispectral and panchromatic images. *IEEE Transactions on Systems, Man, and Cybernetics, Part B (Cybernetics)*, 42 (6), 1693–1704. doi:10.1109/TSMCB.2012.2198810

Zhang, X., *et al*., 2010. Bregmanized nonlocal regularization for deconvolution and sparse reconstruction. *SIAM Journal on Imaging Sciences*, 3 (3), 253–276. doi:10.1137/090746379

Zhang, X., *et al*., 2007. Application of Tikhonov regularization to super-resolution reconstruction of brain MRI images. *In*: *2nd international conference, MIMI 2007*. Beijing: Springer-Verlag, 51–56.

Zhang, Y. and Zhou, Q., 2011. An improved method for POCS superresolution image reconstruction. *In*: *2011 international conference on electronics, communications and control, ICECC 2011*, September 9, 2011–September 11, 2011. Ningbo, China: IEEE Computer Society, 4150–4153.

Zheng, X., *et al*., 2015. A robust channel network extraction method combining discrete curve evolution and the skeleton construction technique. *Advances in Water Resources*, 83, 17–27. doi:10.1016/j.advwatres.2015.05.003

Zhou, Q. and Liu, X., 2004. Analysis of errors of derived slope and aspect related to DEM data properties. *Computers & Geosciences*, 30 (4), 369–378. doi:10.1016/j.cageo.2003.07.005

Zhou, Q. and Zhu, A.-X., 2013. The recent advancement in digital terrain analysis and modeling. *International Journal of Geographical Information Science*, 27 (7), 1269–1271. doi:10.1080/13658816.2013.794281